ACS APPLIED ELECTRONIC MATERIALS

pubs.acs.org/acsaelm Article

Tailing the Magnetoelectric Properties of 2H-MoS_2 by Engineering Covalently Bonded Mo Self-intercalation: Ferromagnetic Materials

Zhaoyong Guan,* Fangyu Zhang, Linhui Lv, Chao Jia, Weiyi Wang, Yanyan Jiang, Xingxing Li, and Ya Su

Cite This: *ACS Appl. Electron. Mater.* 2024, 6, 4066−4079 Read Online

ACCESS | Metrics & More | Article Recommendations | Supporting Information

ABSTRACT: Two-dimensional (2D) intrinsic ferromagnetic (FM) materials play a crucial role in spintronics. Through a systematic research of the 2H-MoS_2 bilayer (BL) with self-intercalation (SI) of Mo atom, we have discovered that SI can introduce a long-range magnetic order, as Mo_{SI} atoms lose electrons. The MoS_2 BLs (Mo_mS_n) with self-intercalated Mo (Mo_{SI}) atoms show antiferromagnetic (AFM) order under a high concentration of Mo_{SI} atoms, where the direct exchange interaction dominates over the superexchange interaction. Mo_mS_n becomes half-metal (HM) with interlayer FM order after Mo's self-intercalation, under lower Mo_{SI} atom concentrations, independent of the stacking orders. Mo_9S_{16}-AA exhibits HM with FM order, with a corresponding Curie temperature (T_c) of 35 K. Mo_mS_n-AA and AB stackings with a lower concentration of Mo_{SI} atoms transform into half semiconductors (HSCs). Moreover, the magnetic anisotropy energies (MAEs) of Mo_9S_{16}-AA and AB stackings are −0.080 and −1.06 meV/f.u., suggesting that the magnetic easy axis (EA) of Mo_mS_n tends to the [100] direction, regardless of the stacking orders. However, the MAEs of Mo_mS_n-AA and AB stackings differ due to variations in the hybridization interaction between Mo's d orbitals. The formation energies of Mo_mS_n change with the chemical potential of S (μ_s) and the concentration of Mo_{SI} atoms. Furthermore, the formation energy (ε_f) monotonically increases as the concentration of Mo_{SI} monotonically increases. Additionally, Mo_mS_n with Mo_{SI} atoms could be synthesized under a higher chemical potential of Mo atom (μ_{Mo}). The Mo_mS_n-AB stackings are always more stable than the AA stackings. Self-intercalated Mo_mS_n exhibits good dynamic and thermal stability at 300 and 600 K, respectively. These findings suggest a promising approach to introducing a modulated long-range FM order and electromagnetic properties into 2H-MoS_2 and other transition metal dichalcogenides (TMDs).

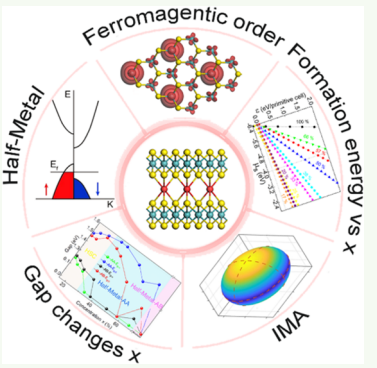

KEYWORDS: *2H-MoS_2, self-intercalation, 2D ferromagnetism, half-metal, magnetic crystal anisotropy, magnetic vdW material, MAE*

INTRODUCTION

Since the discovery of graphene,[1,2] all kinds of two-dimensional (2D) materials,[3,4] such as hexagonal boron-nitride,[5] and transition metal dichalcogenides (TMDs)[6−8] have been unveiled. These 2D materials have attracted much attention, owing to their diverse physical[9] and chemical properties,[4,10] such as Dirac cone,[1] high carrier mobility,[2] and ballistic transport properties.[8] Their versatile characteristics render them indispensable in various fields including nanoelectronics,[6] optoelectronics,[9] photocatalysis,[11] spintronics,[12,13] and energy storage.[14] TMD multilayers can be assembled via van der Waals (vdW) interaction.[15] In addition, TMDs and other 2D materials could form various vdW structures,[15,16] endowing them with diverse remarkable properties.[16] Although pristine TMD layers have amazing features,[4] it is highly desired for them to have novel properties in order to broaden their applications.[16] Strain manipulation is a widely employed strategy in experiments and theory.[8,17] Carrier doping is also a tunable method to manipulate electromagnetic properties.[18] The substitution of transition metal (TM) can modulate magnetoelectronic properties.[19−21] The substitution could also change the conductivity from a normal semiconductor to half-meta (HM) and half semiconductor (HSC),[19] resulting in n-type and p-type semiconductors.[20] Furthermore, substitution can induce transitions from nonmagnetic order to ferromagnetic (FM), antiferromagnetic (AFM), and ferrimagnetic (Ferrim) orders, respectively.[21] Additionally, most 2D materials are inherently nonmagnetic, due to the strong fluctuations at finite temperatures, which prohibit long-range magnetic order in these systems.[22]

Among all kinds of methods, intercalation is a powerful method for tuning the properties of vdW materials,[23] such as electronic properties,[24,25] optoelectronic properties,[26,27] magnetoelectric properties,[28,29] thermoelectric properties,[30] and energy storage characteristics.[31] Apart from foreign atoms,[23−31]

Received: January 9, 2024
Revised: May 18, 2024
Accepted: May 20, 2024
Published: June 1, 2024

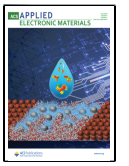

https://doi.org/10.1021/acsaelm.4c00051
ACS Appl. Electron. Mater. 2024, 6, 4066−4079

the native atoms could also work as intercalants. It is named self-intercalation (SI),[32] which has also attracted much attention.[33−37] The self-intercalated structures are more stable than vdW structures, as different layers are connected by self-intercalated atoms.[32] In addition, the native intercalated atoms could affect interlayer magnetic coupling.[29,37,38] In 2019, Prof. Wu found the anomalous Hall effect (AHE) in V_5S_8.[39] In 2020, Prof. Loh first synthesized self-intercalated structures in $TaS(Se)_x$ by performing growth under a high metal chemical potential (μ).[32] Besides that, $V_{11}S_{16}$, $In_{11}Se_{16}$, and Fe_xTe_y could be synthesized under metal-rich condition.[32] AHE has been found in Ta_7S_{12}.[32] In 2020, Prof. Xiang and Zhou found the topological Hall effect in $Cr_{1.2}Te_2$,[40] and magnetic Moié superlattice in Cr_5Te_8,[41] respectively. Prof. Xiang, Liu et al. found perpendicular magnetic anisotropy (PMA) in SI-$CrTe_2$,[42] colossal anomalous Hall effect in Cr_5Te_8,[43] and Néel-type skyrmions in SI−$Cr_{1+\delta}Te_2$,[44] respectively. Prof. Lin constructed a Cr_2Te_3−Cr_5Te_8 lateral heterojunction, which is used to manipulate magnetic moments under different magnitudes of magnetic excitation.[34] Prof. Batzill found that the magnetic properties of $Cr_{(1+\delta)}Te_2$ are maintained in the ultrathin limit. The magnetic anisotropy can be tuned from close to isotropic (δ = 1) to a desirable perpendicular anisotropy for low δ values.[45] Zhang synthesized SI-$NiTe_2$ and predicted superconductivity.[46] In 2023, Prof. Cheng found that $MoSi_2N_4(MoN)_{4n}$ homologous compounds are superconductors.[47] Prof. Zhang constructed the Kagome lattice in SI-1T-FeS_2.[48] Prof. Zhang synthesized 2D triclinic Fe_5Se_8 and monoclinic Fe_3Se_4 phases. They found that 2D Fe_5Se_8 shows intrinsic room-temperature ferromagnetic property, while the ultrathin Fe_3Se_4 presents novel metallic features.[49,50] Prof. Ji found a quenched charge density wave and superconductivity in SI-$NbSe_2$.[33] Moreover, they found a large in-plane upper critical field beyond the Pauli limit by scanning tunneling spectroscopy. Prof. Zheng found the interplay between CDW and superconductivity in SI-TaS_2.[51] Prof. Zhou transformed $PbTe_2$ and $NiTe_2$ into PbTe and NiTe single crystals, respectively, using self-intercalated metal atoms.[52]

The successful experimental realization of SI in 2D materials paves a new way of modulating 2D materials' magnetoelectric properties.[32,33,39−53] Compared with the progress of experiments,[32,33,39−52] theoretical work is rare,[29,35,37,38,54,55] and most works focus on 2D magnetic materials,[29,38−46,49,50,53−56] including VS_2,[39] CGT,[29] CrI_3,[37] $FeCl_2$,[38] $CrTe_2$,[40−45] and Fe_3GeTe_2.[56] These self-intercalated 2D materials have CDW,[51] working as single-atom catalysts,[57] superconductors,[48,51] and extendable piezo/ferroelectricity.[58]

In this article, we systematically investigate the geometry, formation energy, and magnetic and electronic properties of Mo_mS_n using the first-principles method. The Mo_mS_n with AB stacking is more stable than AA stacking. Moreover, the Mo_mS_n are HMs with interlayer FM order, regardless of the stacking configuration with lower Mo_{SI} atom concentration. This shows that the superexchange between Mo and S atoms is stronger than the direct exchange interaction between Mo atoms. Specifically, Mo_9S_{16}-AA exhibits a ferromagnetic HM behavior with a T_c of 35 K. As x is further declined, Mo_mS_n is transformed from HM into HSC. In addition to that, Mo_{SI} atoms could introduce magnetic anisotropy, as the hybridization interaction between Mo atoms' d_{xz} and d_{xy}, d_{xy}, $d_{x^2-y^2}$ orbitals is enhanced. Additionally, different stacking patterns affect the hybridization interaction between Mo atoms' d orbitals, resulting in different MAEs of AA and AB configurations. Both the EAs of AA and AB stackings align along the [100] direction. The ε_f varies with the concentration of the Mo_{SI} atom and μ_s, and Mo_mS_n (with Mo_{SI}) tends to be synthesized under high molybdenum chemical potential (μ_{Mo}). Mo_mS_n also shows excellent dynamic and thermal stability. These findings pave a promising pathway for introducing long-range ferromagnetic order into nonmagnetic materials.

COMPUTATIONAL DETAILS

The calculation of Mo_mS_n is done using the plane-wave basis Vienna Ab initio Simulation Package (VASP) code,[59] based on the density functional theory (DFT). The generalized gradient approximation (GGA) with Perdew−Burke−Ernzerhof (PBE)[60] is adopted. The art of hybrid-functional HSE06[61,62] and LDA + U method[63] are used to deal with the strong-correlated correction to Mo's 3d electrons. The effective on-site Coulomb interaction parameter (U) and exchange interaction parameter (J) are set to be 3.60 and 0.60 eV, respectively. Therefore, the effective U_{eff} (U_{eff}, $U_{eff} = U - J$) is set as 3.0 eV.[64] The geometry optimization, energies with all kinds of magnetic orders, band structure, density of states (DOS), phonon spectrum, ab initio molecular dynamics (AIMD), and MAE are calculated with the LDA + U method. Energies with magnetic order, spin charge densities difference, band structure, and DOS are confirmed by HSE06 functional. The vacuum space in the z-direction is set to 16 Å to avoid virtual interaction. The kinetic energy cutoff is set as 360 eV. The geometries are fully relaxed until the energy and force are converged to 10^{-5} eV and 1×10^{-2} eV/Å, respectively. 6 ×6 × 1, 9 × 9 × 1, and 16 × 16 × 1 Monkhorst−Pack grids[65] are used for the geometry optimization, energy calculation, and DOS calculation, respectively. Spin−orbital coupling (SOC) is also considered in the calculation of the MAE and band structure.

The MAE calculations employ an energy cutoff of 500 eV, with total energy and force convergence criteria set to 1×10^{-8} eV and 1 meV/Å, respectively. Following systematic testing, the corresponding k-grid (18 × 18 × 1) is adopted, without any symmetry constriction, shown in Figure S1. Phonon spectra and DOS are calculated using the finite displacement method, as implemented in the Phonopy Package.[66] A 3 × 3 × 1 cell is adopted in the simulation. The total energy and Hellmann−Feynman force are converged to 10^{-8} eV and 1×10^{-2} eV/Å, respectively. Eight thousand uniform k-points along high-symmetry lines are used to obtain phonon spectra. In order to confirm the structural stability, an AIMD simulation is also performed. The constant moles−volume−temperature (NVT) ensemble with Nosé−Hoover thermostat[67] is adopted at temperatures of 300 and 600 K, respectively. The time step and total time are 1 fs and 10 ps, respectively. In order to eliminate the effect of periodic boundary condition with a relatively smaller system size, a larger supercell (2 × 2 × 1 cell) is adopted in the AIMD simulation. T_c is calculated using the PASP package,[68] developed by Prof. Xiang. The DFT-D2 Grimme method[69] is adopted to account for the weak vdW interaction between layers.

Geometry and Electromagnetic Properties. 50% Mo-intercalated MoS_2 has a stoichiometry of Mo_9S_{16}.[32] The geometries of Mo_9S_{16}-AA and AB stackings are optimized, as shown in Figure 1a−d, respectively. The corresponding lattice parameters ($a = b$) of Mo_9S_{16}-AA and AB stackings are 6.419 and 6.458 Å, respectively. The a of Mo_9S_{16}-AB is a little larger

https://doi.org/10.1021/acsaelm.4c00051
ACS Appl. Electron. Mater. 2024, 6, 4066−4079

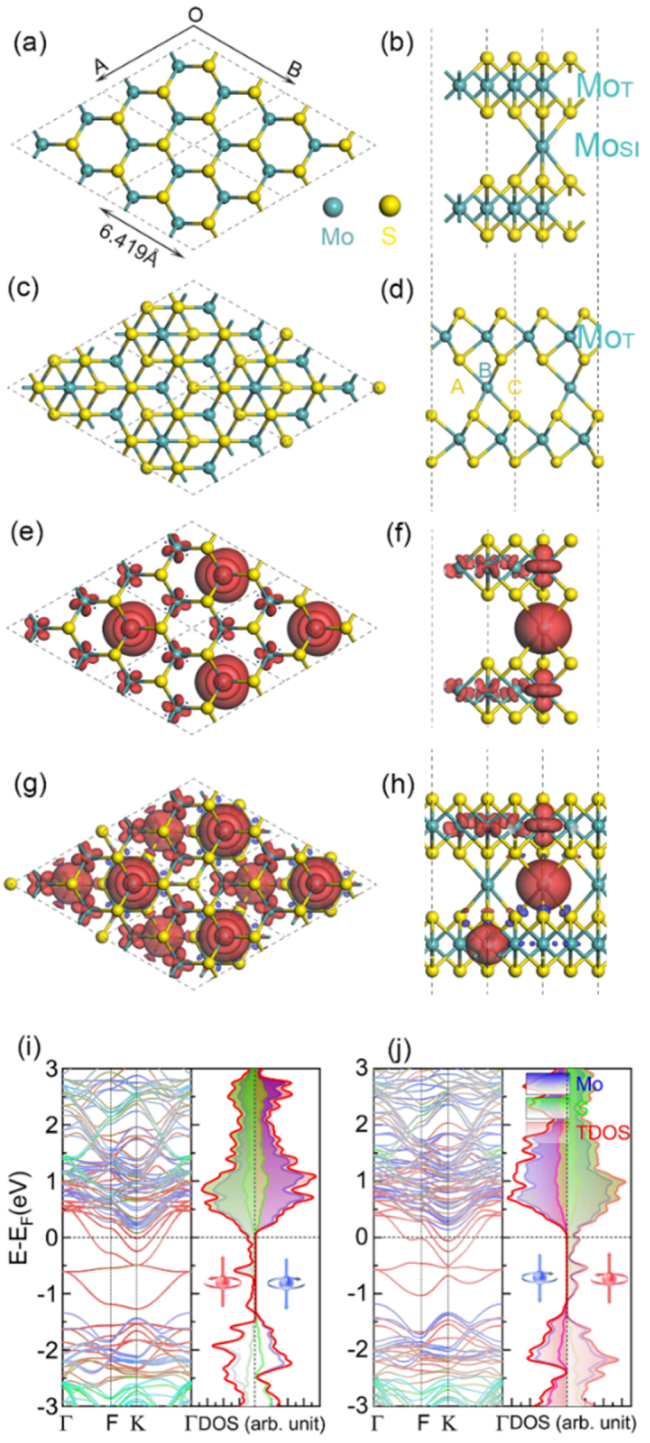

Figure 1. Optimized geometries of Mo_9S_{16}-AA(AB). Illustration of Mo_9S_{16}-AA(AB) structures. (a−d) Top and side views of Mo_9S_{16}-AA (AB) stackings. The corresponding spin charge densities of (e, f) AA and (g, h) AB are calculated. The isovalue is set to 0.06 e/Å^3. (i, j) The band structure and PDOS of Mo_9S_{16}-(i) AA and (j) AB, respectively. The blue, green, and red represent Mo, S-projected, and total DOS, respectively. The cyan and yellow balls represent Mo and S atoms, respectively.

than that of Mo_9S_{16}-AA. In addition to that, the *a* of Mo_9S_{16} is a little larger than that of MoS_2 bilayer (BL) (6.380 Å), as shown in Figure S2a,b. This implies that SI could expand the lattice, as the Mo_{SI} atom is "inserted" into the MoS_2 BL, as shown in Figure S2a−d. Compared with the different intercalated sites A, B, and C, shown in Figure 1d, the Mo_{SI} atom prefers to stay at the B site, which occupies the center of the octahedra composed of six S atoms in the vdW gap, regardless of the stacking patterns. In addition, the original planar structures of MoS_2 monolayer (ML) are maintained. However, there is minor geometry distortion near the S atoms, which are connected to the Mo_{SI} atom, as shown in Figure 1b,d. It is similar to Cr-intercalated CGT,[29] Ta-intercalated TaS_2,[32] and Fe-intercalated $FeCl_2$.[38] Mo_9S_{16}-AA shows the D_{3d} point group, while Mo_9S_{16}-AB shows the C_{3v} point group, which are the same with MoS_2 BL-AA and AB stackings, respectively.[8] The magnetic properties of Mo_9S_{16}-AA and AB patterns are also investigated, as shown in Figure 1e−h, respectively. The magnetic moment (MM) is mainly localized in Mo_{SI} and neighboring Mo atoms (Mo_T). The Mo_{SI} atom in Mo_9S_{16}-AA contributes 3.94 μ_B and Mo_T atoms have 0.52 μ_B, as shown in Figure 1e,g. The Mo_{SI} atom in Mo_9S_{16}-AB contributes 3.68 μ_B, and Mo_T atoms have 0.60 μ_B, as shown in Figure 1f,h, respectively. Besides that, both Mo_9S_{16}-AA and AB patterns have a total MM of 6.00 μ_B. We also calculate the spin densities of Mo_9S_{16}-AA and AB patterns with the art of HSE06, as shown in Figure S3a−d, respectively. The Mo_{SI} atom in Mo_9S_{16}-AA has 3.79 μ_B, while Mo_T atoms contribute 0.36 μ_B, as shown in Figure S3a,b. However, the Mo atoms in Mo_9S_{16}-AB contribute 3.53 μ_B (Mo_{SI}) and 0.37 μ_B (Mo_T), as shown in Figure S3c,d, respectively.

The magnetic properties have been investigated, and the corresponding electronic properties are related to the magnetic order,[29,38] as depicted in Figure 1i,j. The band structure of Mo_9S_{16}-AA and partial density of states (PDOS) are shown in Figure 1i. The spin-α electron is conductive, while the spin-β electron is a semiconductor with an indirect gap of 1.506 eV. Therefore, Mo_9S_{16}-AA is HM. Meanwhile, the spin-β electrons' indirect gap of Mo_9S_{16}-AB is 1.316 eV. Mo_9S_{16}-AB is also HM, as shown in Figure 1j. The states at the Fermi level predominantly originate from Mo atoms, as shown in Figure 1i,g, respectively. The PDOS of Mo_9S_{16}-AA (AB) also confirm the above results, as depicted in the right inset of Figure 1i,j, respectively. The electronic properties are relative to those of d electrons. In order to clarify d electron's orbital occupation, the d orbital projected band structure and PDOS are also calculated, as shown in Figure S4. The states of Mo_9S_{16}-AA and AB stackings at Fermi level are primarily contributed by Mo's d_{z^2} orbital, as indicated in Figure S4. The band structure and PDOS are also calculated by the HSE06 functional, as shown in Figure S3e−h. Mo_9S_{16}-AA and AB stackings are HM, with a direct spin-β electron gap of 1.157 and 1.692 eV, respectively. The states of Mo_9S_{16}-AA with AB stackings at Fermi level are mainly contributed by Mo atoms, shown in Figure S3f,h, which is similar to the LDA + *U* method. Compared with MoS_2 BL, Mo_{SI} and Mo atoms bring additional states in the original gap of MoS_2 BL. The band structures of MoS_2 BL with AA and AB stackings are also calculated, as shown in Figure S2e,f. The corresponding band gaps are 1.50 and 1.48 eV. Consequently, Mo_9S_{16}-AA (AB) stackings exhibit HM characteristics.

Since Mo is TM, the impact of SOC on the electronic properties should be considered. The band structures under SOC with EA oriented along the [100] and [001] directions are also calculated, as presented in Figure S5. Neither Mo_9S_{16}-AA nor Mo_9S_{16}-AB is a normal metal with SOC. The band structure of Mo_9S_{16}-AA and AB stackings with SOC with EA along the [001] direction is different from that along the [100]

https://doi.org/10.1021/acsaelm.4c00051
ACS Appl. Electron. Mater. 2024, 6, 4066−4079

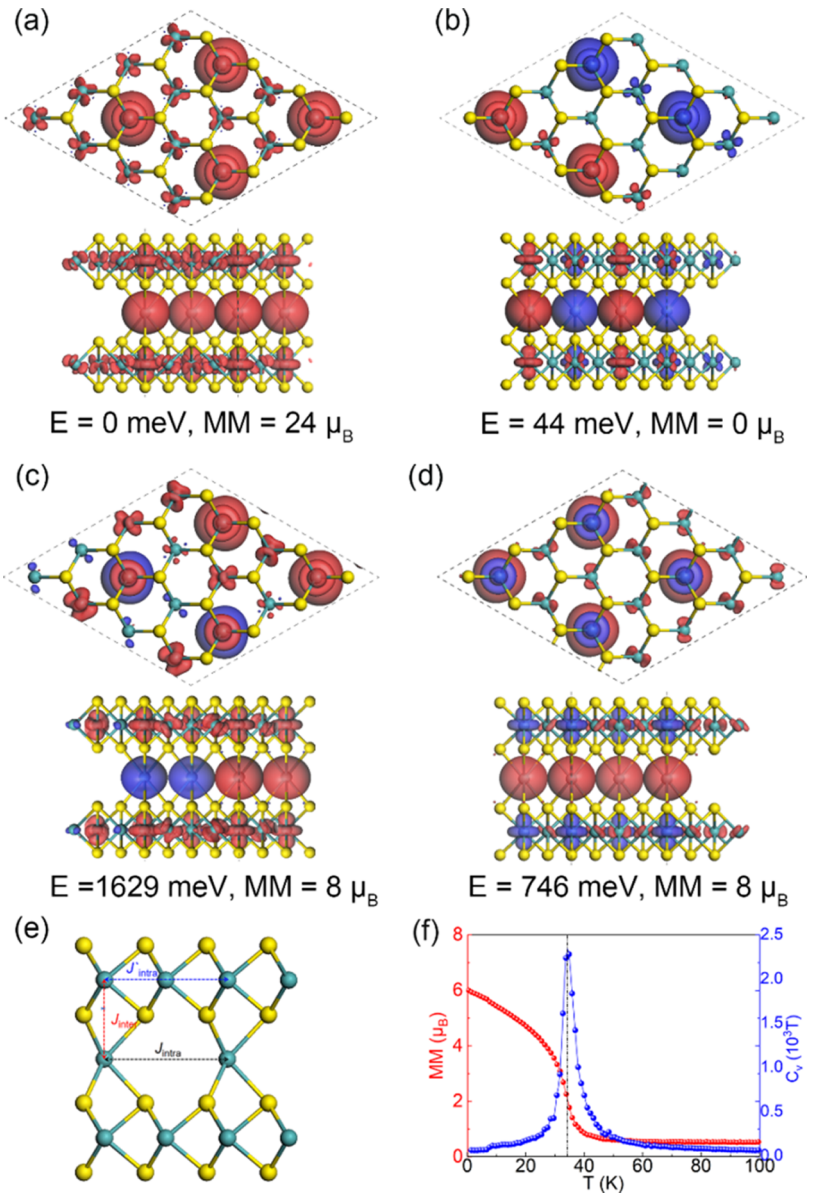

Figure 2. Spin charge densities of Mo_9S_{16}-AA stacking with (a) FM, (b) AFM, (c) Ferrim-I and (d) Ferrim-II orders, respectively. The isovalue is set to 0.04 e/Å^3. (e) Illustration of neighbor, and next neighbor exchange interactions. J_{inter}, J_{intra} and J'_{intra} represent the first, second, and third in-plane nearest-neighbor spin−spin exchange interaction. Specific heat (C_v) (red) and MM (blue) of (f) Mo_9S_{16}-AA vary with respect to the temperature from the Heisenberg model MC simulation.

direction, particularly at Γ and *K* points; more details could be found in the Supporting Information.

In order to confirm the magnetic order, a 2 × 2 × 1 supercell of Mo_9S_{16} is built. The spin charge densities of Mo_9S_{16}-AA (AB) stackings are investigated, as shown in Figures 2a−d, S6, and S7. Both Mo_9S_{16}-AA (AB) stackings show FM order, and the energies of FM order are 44 (AA) and 492 (AB) meV lower than the AFM order (second lowest energy), as shown in Figures 2b and S6. The corresponding MM of FM order is 24.00 μ_B, and Mo_{SI} atoms contribute 3.94 (3.94 × 4) μ_B. The Mo_T atoms (top of Mo_{SI}) have 0.52 (0.52 × 8) μ_B, as shown in Figure 2a. Similar to Mo_9S_{16}-AA stacking with AFM order, Mo_T ferromagnetically couples with the surrounding Mo_{SI} atom, as shown in Figure 2b. However, Mo atoms in the "same layer" (Mo_{ML}) antiferromagnetically couple with other Mo atoms. Mo_{SI} atoms also antiferromagnetically couple with other Mo_{SI} atoms, as shown in Figure 2b. Thus, the total MM equals 0 μ_B, and the energy is 44 meV higher than FM order, as shown in Figure 3b. In addition to that, there are two Ferrim orders: all Mo_{ML} atoms ferromagnetically couple with each other, while Mo_{SI} atoms antiferromagnetically couple with each other, as shown in Figure 2c. This ferrimagnetic (Ferrim-I) order with the highest energy in the considering orders has an MM of 8.0 μ_B. All Mo_{ML} and Mo_{SI} atoms ferromagnetically couple with Mo_{ML} and Mo_{SI} atoms, respectively, while Mo_{ML} and Mo_{SI} atoms antiferromagnetically couple with each other, which is defined as the Ferrim-II order, shown in Figure 2d. All energies with different magnetic orders are also calculated by the HSE06 functional, which are consistent with the PBE + *U* method, as shown in Figure S6.

J_{inter} denotes the nearest-neighbor exchange constants of the interlayer, as shown in Figure 2e. J_{intra} and J'_{intra} are the second-nearest-neighbor exchange constants. $J > 0$ denotes the ferromagnetic order, while $J < 0$ represents the antiferromag-

https://doi.org/10.1021/acsaelm.4c00051
ACS Appl. Electron. Mater. 2024, 6, 4066−4079

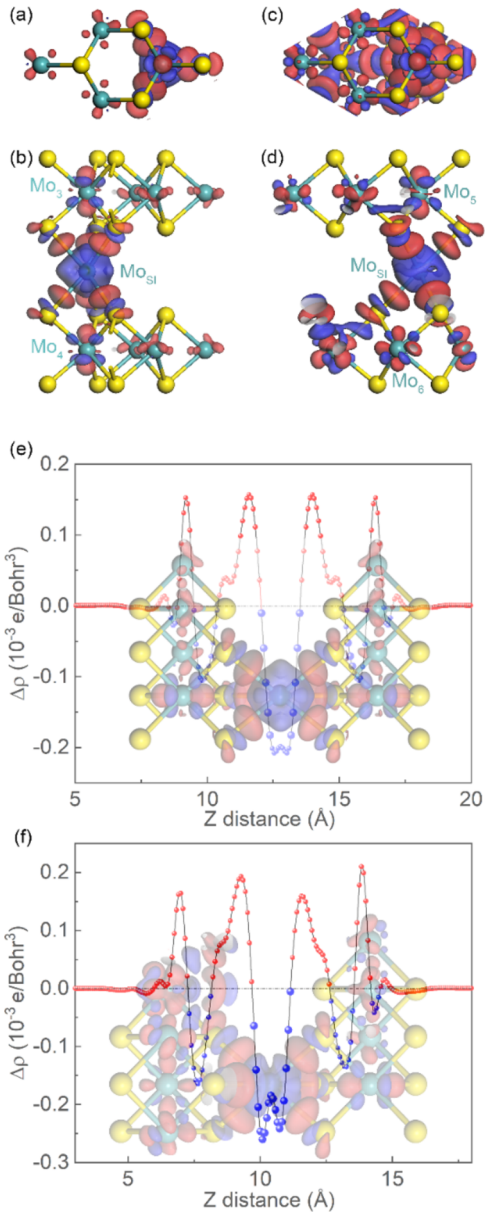

Figure 3. Charge density difference of (a, b) Mo_9S_{16}-AA and (c, d) AB. The red and blue represent the accumulation and depletion of electrons, respectively. The averaged planner electrical charge density difference along the *c* direction of (e) Mo_9S_{16}-AA and (f) AB, respectively. The red and blue dots represent the accumulation and depletion of electrons, respectively.

netic order. The J_{inter}, J_{intra}, and J'_{intra} of Mo_9S_{16} are calculated with the following equations

$$E_{FM} = E_0 - 8J_{inter} - 12J_{intra} - 24J'_{intra} \quad (1)$$

$$E_{AFM} = E_0 - 8J_{inter} + 4J_{intra} + 8J'_{intra} \quad (2)$$

$$E_{Ferrim\text{-}I} = E_0 + 4J_{intra} - 24J'_{intra} \quad (3)$$

$$E_{Ferrim\text{-}II} = E_0 + 8J_{inter} - 12J_{intra} - 24J'_{intra} \quad (4)$$

The J_{inter}, J_{intra}, and J'_{intra} values of Mo_9S_{16}-AA stacking are 46.6, 19.6, and −151.5 meV, respectively. The formulas are shown in eqs S5−S8, and more details about the calculation of *J* are shown in the Supporting Information. The total MM equals 6.0 μ_B at 0 K, as shown in Figure 2f. As the temperature increases, the MM monotonically decreases, while the magnetic susceptibility first increases. Then, the magnetic susceptibility reaches the largest value of 560, and the corresponding T_c is 35 K, as shown in Figure 2f. The T_c is evaluated with the following equation

$$H = -\sum_k \sum_{i>j} \sum_j J_k S_i \cdot S_j + \sum_i D_i S_{iz}^2 \quad (5)$$

where J_k denotes the three different exchange-coupling parameters presented in Figure 2e. S_i and S_j are the spin of Mo_{SI} or Mo_T atoms. D_i is the magnetic anisotropy parameter.

Similar to Mo_9S_{16}-AB with FM order, each Mo_T atom has 0.60 (total 0.60 × 4) μ_B, while Mo_{SI} atoms have 3.94 μ_B, as shown in Figures 1b and S7. The Mo atoms in one layer have 1.20 (total 1.20 × 4) μ_B, while other Mo atoms in the other layer have 0.04 (total 0.04 × 4) μ_B, as shown in Figures 1b and S7a. Mo_T atoms ferromagnetically couple with neighboring Mo_{SI} atoms under AFM order, and the corresponding MMs are 0.50 (0.50 × 2), and − 0.50 (−0.50 × 2) μ_B, respectively. Mo_{SI} atoms have 3.94 and −3.94 μ_B, as shown in Figure S7b, respectively. The total MM is equal to 0 μ_B. The J_{inter}, J_{intra}, and J'_{intra} of Mo_9S_{16}-AB stacking are 62, 138.8, and −9.7 meV, respectively. The detailed formulas are provided in eqs S9−S16, and more details about the calculation of *J* are shown in the Supporting Information.

Charge Density Difference. Both MoS_2 ML and BL are nonmagnetic semiconductors. Why could the Mo_{SI} atom introduce long-order magnetic order? In this section, we want to clarify this issue by analyzing the charge density difference, as shown in Figure 3. The Mo_{SI} atom shows a different chemical environment from Mo_{ML} atoms. The corresponding charge density difference of Mo_9S_{16}-AA (AB) is shown in Figure 3a−d, respectively. It is evident that charges predominantly accumulate and deplete in self-intercalated areas, as shown in Figure 3a,b. According to Bader analysis,[70] the Mo_{SI} atom of AA stacking has 4.66e electrons. Therefore, the Mo_{SI} atom loses 1.34e electrons to the connected S atoms, and a similar phenomenon also appears in SI-CGT[29] and SI−CrI_3.[37] In contrast, Mo_3 and Mo_4 (adjacent to S atoms connected with the Mo_{SI} atom) have 4.41e electrons. As a result, there are 1.59e electrons transferring from Mo_3 and Mo_4 to the surrounding S atoms, as shown in Figure 3a,b. In AB stackings, the Mo_{SI} atom has 4.46e electrons, while the Mo atoms (Mo_5, Mo_6) near S atoms have 4.44 and 4.49e electrons, respectively. Consequently, Mo_{SI} and neighboring Mo_5, Mo_6 atoms lose 1.54, 1.56, and 1.51e electrons, respectively, as shown in Figure 3. Compared with AA stacking, the Mo_{SI} atom in AB stacking loses more electrons, as shown in Figure 3. In order to clarify this point, the averaged planner electrical potential along the *c* direction of Mo_9S_{16}-AA(AB) stackings is calculated, as shown in Figure 3e,f, respectively. It can be concluded that the averaged planner electrical potential curves are symmetric (AA) and antisymmetric (AB), respectively, originating from the different geometries of AA and AB stackings. The largest charge density difference of Mo_9S_{16}-AB is 0.260 × 10^{-3} e/Bohr^3, which is larger than the AA of 0.207 × 10^{-3} e/Bohr^3.

Magnetic Anisotropy Properties. MAE indicates that the electron needs energy to switch from EA (soft axis) to the other direction (hard axis). When the MAE is larger, it indicates that electrons need more energy to switch from EA to the hard axis. As Mo_9S_{16}-AA(AB) have D_{3d} and C_{3v} point

https://doi.org/10.1021/acsaelm.4c00051
ACS Appl. Electron. Mater. 2024, 6, 4066−4079

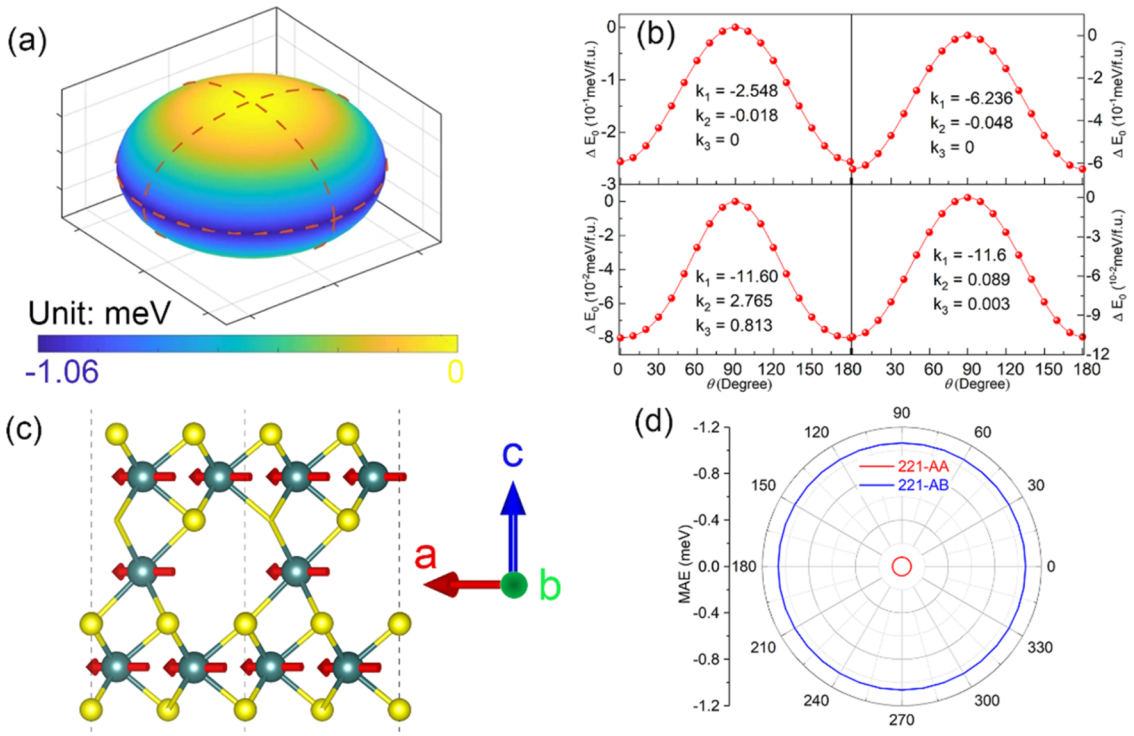

Figure 4. (a) ΔE_0 with x of 50% changes with θ and Ψ. (b) ΔE_0 of Mo_7S_{12}-AA (AB)-SI and Mo_9S_{16}-AA (AB) changes with θ. (c) EA is along the [100] direction. (d) ΔE_0 of Mo_9S_{16}-AA(AB) changes with Ψ.

groups, the corresponding energy (ΔE_0) along a certain direction (θ, ϕ) can be calculated as[29]

$$\Delta E_0 = K_1 \cos^2\theta + K_2 \cos^4\theta + + K_3 \cos^6\theta + K_4 \cos 3\phi \quad (6)$$

$$\Delta E_0 = E - E_{[001]} \quad (7)$$

where $E_{[001]}$ represents the energy along [001] direction, as shown in Figure 4a–d. K_1, K_2, and K_3 represent the quadratic, quartic, and sextic (six degree) contributions to the MAE, respectively. Similar to the geometries with high symmetry,[71] energy difference (ΔE_0) is independent of the in-plane azimuthal angle ϕ, as shown in Figure 4d. Therefore, K_4 equals 0, as shown in Figure 4a,b. Equation 6 is simplified into the following equation

$$\Delta E_0 = K_1 \cos^2\theta + K_2 \cos^4\theta + K_3 \cos^6\theta \quad (8)$$

ΔE_0 changes as a function of the polar angle θ, as shown in Figure 4b. For $Mo_{19}S_{36}$ with a higher concentration (x = 33.33%), the sextic part to the MAE could be negligible, as shown in Figure 4b. Consequently, eq 8 is simplified into the following equation

$$\Delta E_0 = K_1 \cos^2\theta + K_2 \cos^4\theta \quad (9)$$

ΔE_0 (x = 33.33%) with AA and AB stackings follow the equations ΔE_0 (10^{-1} meV) = $-6.236\cos^2\theta - 0.048\cos^4\theta$ and ΔE_0 (10^{-1} meV) = $-2.548\cos^2\theta - 0.018\cos^4\theta$, respectively. As x is further decreased to 25% ($Mo_{33}S_{64}$), ΔE_0 with AA and AB stackings follow the equations ΔE_0 (10^{-2} meV) = $-11.60\cos^2\theta + 2.765\cos^4\theta + 0.813\cos^6\theta$ and ΔE_0 (10^{-2} meV) = $-11.60\cos^2\theta + 0.089\cos^4\theta + 0.003\cos^6\theta$, respectively. MAE and MCA energies could be calculated using the following equations

$$\mathrm{MAE} = E_{[100]} - E_{[001]} \quad (10)$$

$$\mathrm{MCA} = E_{[100]} - E_{[001]} = \mathrm{MAE}/S \quad (11)$$

$E_{[100]}$ represents the energy with magnetic axis along the [100] direction. S is the area of the supercell. The MAEs of Mo_7S_{12} (57.73%) and Mo_9S_{16} are −0.257 (AA), −0.629 (AB), −0.080 (AA), and −1.064 (AB) meV, respectively. The corresponding MCA energies are −0.058 (Mo_7S_{12}-AA), − 0.140 (AB), −0.024 (Mo_9S_{16}-AA), and −0.207 (AB) erg/cm^2. A negative MAE implies that EA points to the in-plane direction, resulting in in-plane magnetic anisotropy (IMA), as shown in Figure 4c. Compared with nonmagnetic MoS_2−BL (MAE = 0 meV), the MCA of Mo_mS_n is enhanced, which indicates that Mo_{SI} atoms are introduced into the system. A similar trend appears in SI-$CrTe_2$.[42] The MAE and MCA are related to the stacking configuration, the reason for which will be discussed in the following section.

Magnetocrystalline Anisotropy. In order to clarify the atomic orbital contribution to MAE, the tight-binding and second-order perturbation theory is adopted to calculate the MAE. According to the canonical formulation,[71,72] the MAE of each atom could be evaluated using the equation

$$\mathrm{MAE}_i = \left[\int E_f(E - E_F)[n_i^{[100]}(E) - n_i^{[001]}(E)]\right] \quad (12)$$

where MAE_i represents the MAE of the ith atom. $n_i^{[100]}(E)$ and $n_i^{[001]}$ are the DOS of the ith atom with EA along the [100] and [001] directions, respectively. Mo_mS_n-AA and AB stackings have D_{3d} and C_{3v} groups; therefore, the energies with EA along [100] and [010] directions are the same.[71,72] Thus, only the [100] direction is considered here. Furthermore, total MAE could be rewritten as the sum of $\mathrm{MAE}_i/\mathrm{MAE}_{tot} = \sum_i \mathrm{MAE}_i$.[72−74] According to the second-order perturbation theory,[73−75] MAE could be obtained by the sum of the following terms[75,76]

https://doi.org/10.1021/acsaelm.4c00051
ACS Appl. Electron. Mater. 2024, 6, 4066−4079

$$\Delta E^{--} = E_x^{--} - E_z^{--} = \xi^2 \sum_{o^+,u^-} (|\langle o^-|L_z|u^-\rangle|^2 - |\langle o^-|L_x|u^-\rangle|^2)/(E_u^- - E_o^-) \quad (13)$$

$$\Delta E^{-+} = E_x^{+-} - E_z^{+-} = \xi^2 \sum_{o^+,u^-} \left(|\langle o^+|L_z|u^-\rangle|^2 - |\langle o^+|L_x|u^-\rangle|^2\right)/(E_u^- - E_o^-) \quad (14)$$

where + and − are the electrons of spin-α and spin-β, and ξ, L_x, and L_z are the SOC constant, with angular momentum operators along the [100] and [001] directions, respectively. u and o stand for unoccupied and occupied states. E_o and E_u represent the energies of the occupied and unoccupied states, respectively. MAE mainly comes from the contribution of spin−orbital matrix elements and energy difference. According to eq 12, MAE is related to the intensity of DOS near the Fermi level. Besides that, the matrix element differences ($|\langle o^-|L_z|u^-|^2 - |\langle o^-|L_x|u^-\rangle|^2$ and $|\langle o^+|L_z|u^-|^2 - |\langle o^+|L_x|u^-\rangle|^2$) for d and p orbitals are calculated, as shown in Tables 1 and 2,

Table 1. Matrix Differences for d Orbitals between Magnetization along [001] and [100] Directions in eqs 9 and 10[71−73]

			o^+					o^-		
u^-	d_{xy}	d_{yz}	d_{z^2}	d_{xz}	$d_{x^2-y^2}$	d_{xy}	d_{yz}	d_{z^2}	d_{xz}	$d_{x^2-y^2}$
d_{xy}	0	0	0	1	−4	0	0	0	−1	4
d_{yz}	0	0	3	−1	1	0	0	−3	1	−1
d_{z^2}	0	3	0	0	0	0	−3	0	0	0
d_{xz}	1	−1	0	0	0	−1	1	0	0	0
$d_{x^2-y^2}$	−4	1	0	0	0	4	−1	0	0	0

Table 2. Matrix Differences for p Orbitals between EA along [001] and [100] Directions in eqs 9 and 10[71−73]

		o^+			o^-	
u^-	p_y	p_z	p_x	p_y	p_z	p_x
p_y	0	1	−1	0	−1	1
p_z	1	0	0	−1	0	0
p_x	−1	0	0	1	0	0

respectively.[71−73] To further interpret the changes in MAE with stacking patterns, the atom-orbital-resolved MAE of Mo_9S_{16} is shown in Figure 5a−c (AA) and Figure 5d−f (AB), respectively. The total MAEs of Mo_9S_{16}-AA and AB stackings are −0.08 and −1.06 meV, respectively. S atoms contribute 0.12 (AA) and 0 meV (AB) to the total MAE, while Mo_{BL} and Mo_{SI} atoms contribute −0.28 (AA), 0.08 (AA), −0.29 (AB), and −0.76 meV (AB), as shown in Figure 5a−e, respectively. For Mo_9S_{16}-AA stacking, the atomic hybridization between Mo_{BL}'s occupied spin-α $d_{x^2-y^2}$ and unoccupied spin-β d_{xy} orbitals contributes to IMA (−0.253 meV), which corresponds to the matrix difference −4 for d orbitals,[72] as shown in Figure 5a and Table 1. Moreover, the atomic hybridization between Mo_{SI}'s occupied spin-α $d_{x^2-y^2}$ and unoccupied spin-β d_{xy} orbitals contributes to IMA (−0.253 meV), which corresponds to the matrix difference −4 for d orbitals,[72] as shown in Figure 5b. Furthermore, the atomic hybridization between S's unoccupied spin-β p_y and occupied spin-α p_z orbitals corresponds to the matrix difference 1,[73] as shown in Figure 5c and Table 2.

Compared with AA stacking, the MAE of AB stacking is mainly contributed by Mo_{BL} and Mo_{SI} atoms. S atoms' contribution could be ignored. The atomic hybridization between the Mo_{BL} of AB stacking-occupied spin-α $d_{x^2-y^2}$ and unoccupied spin-β d_{xy} orbitals contributes to IMA (−2.2 meV), which corresponds to the matrix difference −4 for the d orbitals,[71] as shown in Figure 5e. On the contrary, the hybridization between the occupied spin-α d_{z^2} orbitals and unoccupied spin-β d_{yz} orbitals makes a contribution to PMA (1.11 meV), which corresponds to the matrix difference 3 for d orbitals, as shown in Figure 5e and Table 1. Mo_{BL} atoms make a similar contribution to MAE. The different MAEs of AA and AB stackings should be caused by the different Mo_{SI}'s hybridization between $d_{x^2-y^2}$ and d_{xy}, d_{z^2} and d_{yz} orbitals, which originates from different geometries.[29]

Dynamic and Thermal Stability. The dynamic stability of AA (AB)-SI configurations is confirmed via phonon dispersion curves and phonon DOS (PHDOS), which show no obvious imaginary phonon modes. The phonon band structure and PHDOS of Mo_7S_{12}, Mo_9S_{16}, and $Mo_{19}S_{36}$-AA(AB) are calculated and presented in Figure 6a−f. The highest vibrational frequency of Mo_7S_{12}-AA is 12.803 THz, while Mo_9S_{12} exhibits a high vibrational frequency of 13.06 THz, as shown in Figure 6b. This indicates that the contribution to the low-frequency part ($0 < \varepsilon < 6$ THz) mainly comes from Mo atoms' contribution. On the contrary, S atoms make the main contribution to the middle-frequency part ($6 < \varepsilon < 10$ THz) and much contribution to the high-frequency part ($10 < \varepsilon <$ 13.8 THZ). This distribution of vibrational modes highlights the distinct roles of Mo and S atoms in the dynamic properties of the material.

The thermal stability of Mo_mS_n is evaluated with AIMD. To examine the geometric stability, we also perform AIMD simulation at 300 and 600 K, as shown in Figures 6 and S8. The fluctuation in total energies is also evaluated, with total energies fluctuating around −449.1, −449.3, −596.2, and −596.4 eV at 300 K, as shown in Figure 6g−i, respectively. The random snapshots of geometry further confirm the essential structural integrity shown in the inset of Figure 6g−i. Mo_mS_n under a higher temperature of 600 K is also simulated, and more simulations of $Mo_{33}S_{64}$ (with lower x) are performed, as shown in Figure S8c,d, in the Supporting Information. There is no obvious structure distortion found. Consequently, Mo_mS_n should be stable at 300 and 600 K.

Magnetic Order Change with *x*. In the above section, the energies of Mo_9S_{16} -AA (AB) stackings are calculated, and it can be found that AB stacking has a lower energy than AA stacking. For other concentrations (the geometries are shown in Figures S9a−d and S10a−h), AA stackings always have a higher energy than AB stackings, as shown in Figure 7a. The energy difference of $Mo_{20}S_{36}$ between AA and AA (Figure S10c) and AB stackings (Figure S10d) with magnetic order ($\Delta E_{AA\text{-}AB} = E_{AA} - E_{AB}$) is 0.053 eV; on the contrary, the $\Delta E_{AA\text{-}AB}$ of Mo_7S_{12} (shown in Figure S10e,f) reaches the largest value of 0.405 eV. Subsequently, $\Delta E_{AA\text{-}AB}$ monotonically decreases as x decreases, as depicted in Figure 7a. Specifically, $\Delta E_{AA\text{-}AB}$ is 0.39, 0.217, and 0.01 eV for Mo_9S_{16}, $Mo_{19}S_{36}$, and $Mo_{51}S_{100}$, respectively.

The AB stackings always have a lower energy, regardless of the stacking patterns; yet, the magnetic order is related to the stacking orders, as illustrated in Figure 7b. The Mo_mS_n with AB

https://doi.org/10.1021/acsaelm.4c00051
ACS Appl. Electron. Mater. 2024, 6, 4066−4079

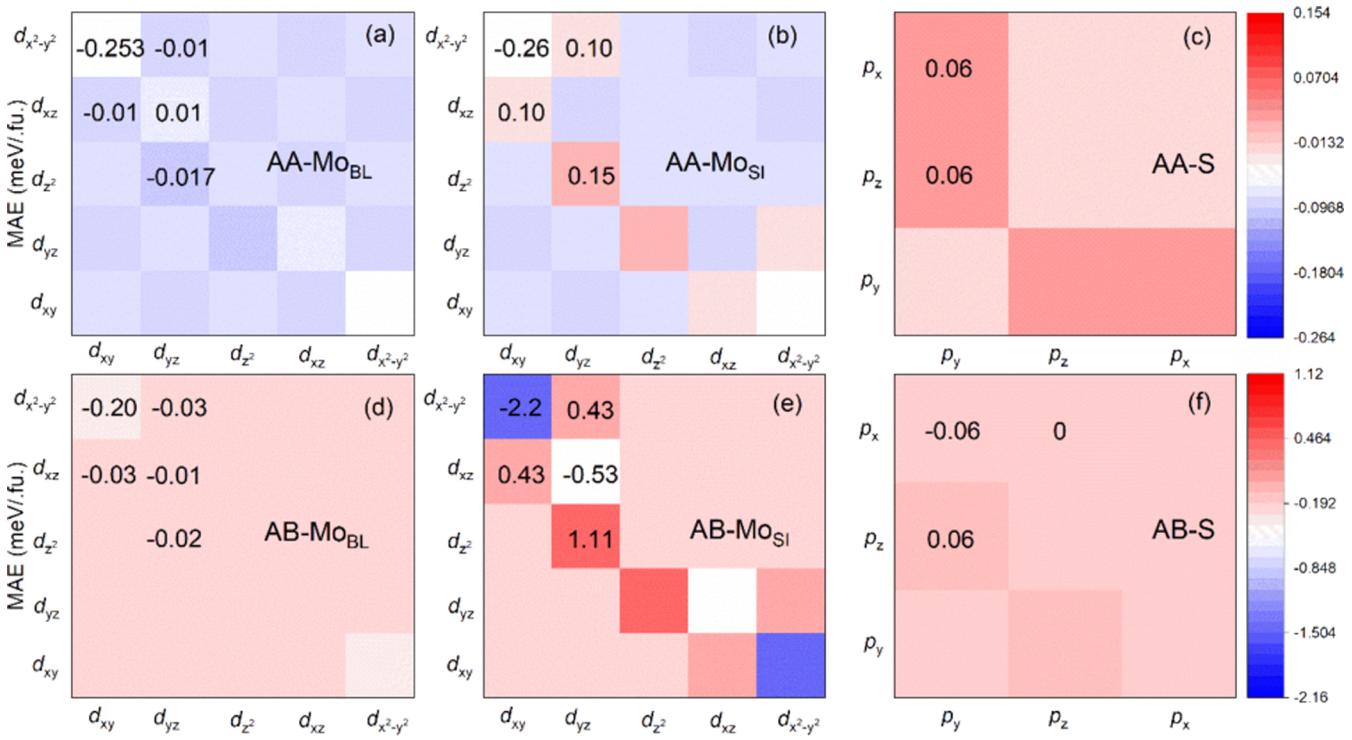

Figure 5. Orbital-resolved MAE of Mo_9S_{16}-AA (AB). (a) Mo_{BL}, (b) Mo_{SI}, (c) S in Mo_9S_{16}-AA, (d) Mo_{BL}, (e) Mo_{SI}, and (f) S in Mo_9S_{16}-AB orbital-resolved MAE.

stackings prefer AFM order for higher concentrations of x ($\geq$57.8%), while AA stackings are dependent on stacking patterns. When x is less than 50%, Mo_mS_n presents FM order, independent of stacking orders. Mo_mS_n with AA stackings shows FM order apart from a concentration of 100%. $Mo_{20}S_{36}$-AA have the smallest $\Delta E_{AA\text{-}AB}$ of −0.09 eV. As x further decreases, the corresponding distance ($d_{Mo_{SI}}$) between Mo_{SI} atoms is increased, and the direct exchange interaction is also obviously weakened. As a result, Mo_mS_n-AA shows FM order. When x is decreased to 25%, $d_{Mo_{SI}}$ is increased to 12.758 Å. The direct exchange interaction between Mo_{SI} atoms significantly weakens, as the direct exchange interaction declines more quickly. Therefore, Mo_9S_{16} shows FM order, but the corresponding ΔE_{AA-AB} is also decreased to −0.003 eV, as shown in Figure 7b. For AB stackings with high concentration ($x \geq 57.73\%$), the $d_{Mo_{SI}}$is 5.554 (Mo_7S_{12}) and 5.559 ($Mo_{20}S_{36}$) Å, as shown in Figures S11a−d and S12a−d, respectively. Therefore, the superexchange interaction between Mo_{SI} atoms is weaker than the direct exchange interaction between Mo_{SI} and Mo_{BL} atoms, leading to AFM order in Mo_mS_n. As $d_{Mo_{SI}}$ decreases, the direct exchange interaction declines more rapidly than the superexchange interaction. Consequently, Mo_mS_n with AB stackings shows FM order, which is similar to that with AA stackings. Mo_9S_{16} has the smallest ΔE_{FM-AFM} of −0.492 eV, marked with a star in Figure 7b. As x is further deduced, the corresponding $d_{Mo_{SI}}$ is increased, weakening the superexchange interaction. Therefore, ΔE_{FM-AFM} are further decreased to −0.025 ($Mo_{15}S_{28}$) and −0.095 ($Mo_{19}S_{36}$) eV. The energies with different magnetic orders of $Mo_{19}S_{36}$ are presented in Figure S11a−d.

Formation Energy Change with *x*. The ε_f values of 2D materials usually change with μ, and the ε_f is defined as follows

$$\varepsilon_f = E_{total} - m \times \mu_{Mo} - n \times \mu_S \quad (15)$$

$$\mu_{Mo} + 2\mu_S = \varepsilon_{MoS_2} \quad (16)$$

where E_{total} and ε_{MoS_2} represent the total energy and energy of the supercell, respectively. The μ_{Mo} and μ_S represent the chemical potential of Mo and S atoms, respectively. m and n represent the number of Mo and S atoms in Mo_mS_n, respectively. The value of ε_{MoS_2} is −18.091 eV, calculated with the PBE + U method. Equations 15 and 16 could be represented by the following equations

$$\mu_{Mo} = \varepsilon_{MoS_2} - 2\mu_S \quad (17)$$

$$\begin{aligned}\varepsilon_f &= E_{total} - m \times \mu_{Mo} - n \times \mu_S \\ &= E_{total} - m \times (\varepsilon_{MoS_2} - 2\mu_S) - n \times \mu_S \\ &= E_{total} - m \times \varepsilon_{MoS_2} + (2m - n) \times \mu_S\end{aligned} \quad (18)$$

$$\varepsilon = \varepsilon_f/[(m-1)/2] = 2\varepsilon_f/(m-1) \quad (19)$$

The ε_f is related to the μ_{Mo} and μ_S, as shown in eq 15; yet, ε_f is only related to μ_S as shown in eq 18. Figure 8 shows the ε_f of nine concentrations as a function of the chemical potential of sulfur, μ_S, ranging from 2.4 eV below $\mu_{S_{bulk}}$ to 2.0 eV above it. It can be found that x tends to be smaller under most experimental conditions. For most cases, ε increases as x increases, as shown in Figure 8a. Most of all, when x is quite large ($x \geq 50\%$), ε grows rapidly as μ_S increases. When the environment becomes rich in sulfur (higher μ_S), the ε increases quickly and the corresponding ε also grows rapidly. Taking μ_S = −2.4 eV as an example, the corresponding ε is 2.730 (66.67%, Figure 8c), 1.155 (37.80%, Figure 8f), 0.899

https://doi.org/10.1021/acsaelm.4c00051
ACS Appl. Electron. Mater. 2024, 6, 4066−4079

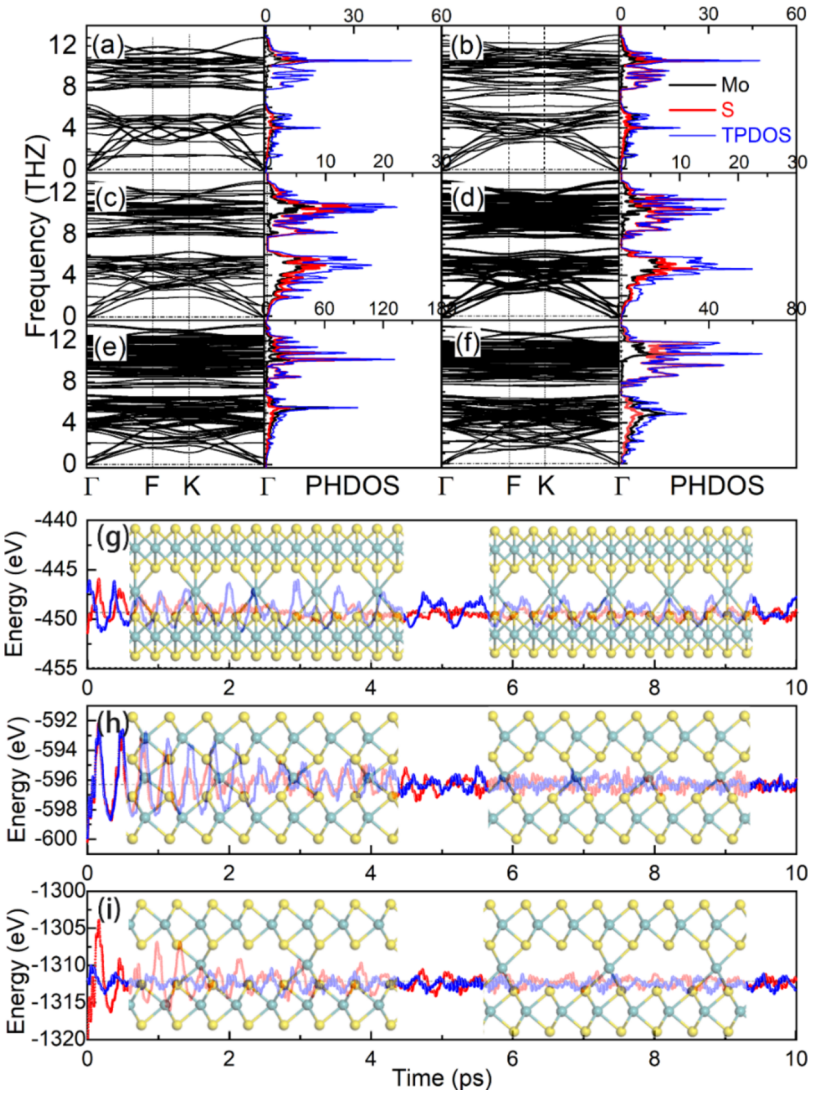

Figure 6. Phonon band and PHDOS of Mo_7S_{12} with (a) AA, (b) AB patterns, Mo_9S_{12}-(c) AA, (d) AB, $Mo_{19}S_{36}$-(e) AA, and (f) AB stackings. The black, red, and blue lines represent Mo, S, and total PHDOS, respectively. The energies of (g) Mo_7S_{12}, (h) Mo_9S_{16}, and (i) $Mo_{19}S_{36}$-AA(AB) change with time. The red and blue lines represent the energies of AA and AB stackings, respectively.

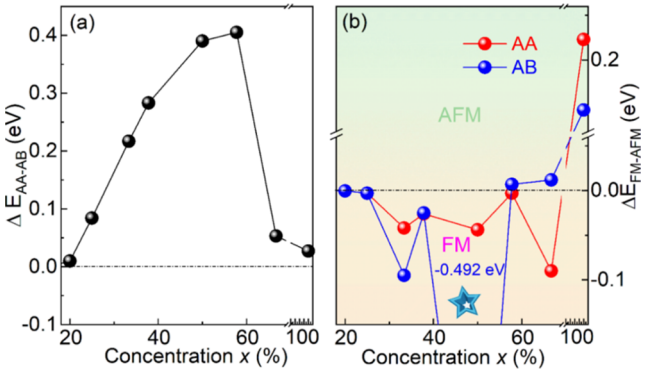

Figure 7. (a) Energy difference between AA and AB stackings, and (b) ΔE_{FM-AFM} change with x. The red and blue lines with dots present AA and AB stackings, respectively. The star represents the smallest ΔE_{FM-AFM}.

(33.33%, Figure 8g), 0.403 (25%, Figure 8h), and 0.319 (20%, Figure 8i) eV/pcell.

When a larger x value is achieved, the corresponding ε becomes larger. This implies that these structures require more energy to form Mo_mS_n. Therefore, Mo_mS_n with higher x values are not easily synthesized in the experiments. However, ε monotonically decreases as μ_S decreases, indicating that these structures are more likely to form in a molybdenum-rich environment (higher μ_{Mo}). Taking $\mu_S = -4.8$ eV as an example, the corresponding ε values are 1.436 (66.67%), 0.470 (37.80%), 0.365 (33.33%), 0.103 (25%), 0.124 (20%), and 0.912 (16.67%) eV/pcell. When μ_S is further decreased to −6.4 eV (molybdenum rich), the corresponding ε values are 0.062, −0.008, 0.125, 0.010, −0.097, −0.004, and 0.002 eV/pcell. This indicates that SI−Mo_mS_n could be synthesized under a highly rich molybdenum environment.[32] There is little difference in the lattice parameters between AA and AB stackings, as shown in Figure S13a,b. Consequently, the effect of strain on ε_f could be ignored. In a word, the formation energies of AA and AB stackings are similar to each other, as shown in Table S1 in the Supporting Information.

Charge Transfer (ΔQ) and Magnetic Properties Change with x. In the previous section, the ΔQ values

https://doi.org/10.1021/acsaelm.4c00051
ACS Appl. Electron. Mater. 2024, 6, 4066−4079

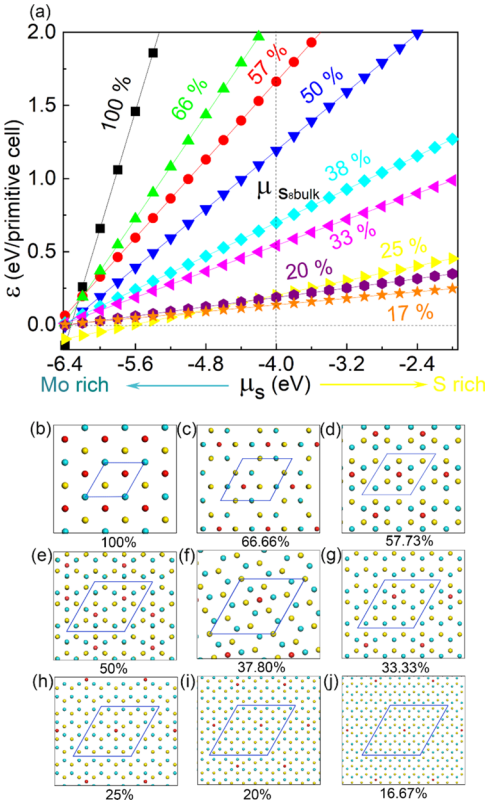

Figure 8. (a) ε as a function of μ_S. The black, green, red, blue, cyan, pink, yellow, purse, and orange dots represent the formation of (b) Mo_3S_4, (c) $Mo_{20}S_{36}$, (d) Mo_7S_{12}, (e) Mo_9S_{16}, (f) $Mo_{15}S_{28}$, (g) $Mo_{19}S_{36}$, (h) $Mo_{33}S_{64}$, (i) $Mo_{51}S_{100}$, and (j) $Mo_{73}S_{144}$ with AB-stackings, respectively. The cyan, red, and yellow balls represent Mo_{BL}, Mo_{SI}, and S atoms, respectively.

between Mo_{SI} and S atoms were calculated. MM mainly localizes at Mo_{SI} atoms, as shown in Figures 1, 2, S6, S7a−d, S11, and S12a−d. The ΔQ and MM of SI-MoS_2 with an x of 50% have been calculated, as shown in Figure S14. The total MM is mainly contributed by Mo_{SI} atoms, with nearby Mo atoms contributing minimally, as illustrated in Figure S12a−d. At a high x of 100%, Mo_{SI} atoms lose 1.38 (AA) and 1.42 (AB) e electrons, resulting in MMs of 4.65 and 4.59 μ_B. As x is decreased to 66.67%, there are 1.26 (AA) and 1.51(AB) e electrons transferred from Mo_{SI} atoms, yielding MMs of Mo_{SI} of 4.74 (AA) and 4.49 (AB) μ_B, as shown in Figure S11a,b. When x is further reduced to 33.33%, the corresponding ΔQ is 1.22 (AA) and 1.41 (AB) e electrons. The corresponding MM is 4.78 (AA) and 4.59 (AB) μ_B, respectively. The spin charge densities of $Mo_{19}S_{36}$ are displayed in Figure S11a−d. Compared with Mo_9S_{16}, the MM of $Mo_{19}S_{36}$ tends to localize at the Mo_{SI} and Mo_T atoms. As x is decreased to 16.67%, the corresponding MM is 4.62 (AA) and 4.40 (AB) μ_B. The total MM of the cell is 6.00 μ_B, except for an x of 100%. The MM of Mo_{SI} with AA stacking is always larger than that of AB stacking due to the larger charge transfer of AB stackings, as shown in Figure S14. Furthermore, ΔQ and x follow a linear relationship, as shown in eqs S17−20, in the Supporting Information. It could be concluded that ΔQ first increases and then suddenly drops at an x of 33.33%. After this, ΔQ increases, following the reduction of x.

Electronic Properties Change with *x*. In the previous section, the magnetoelectronic properties of Mo_9S_{16}-AA(AB) were investigated. What are the characteristics of SI-MoS_2 with a lower concentration? The corresponding band structures are shown in Figure 9. First, Mo_3S_4-AA (AB) are investigated and

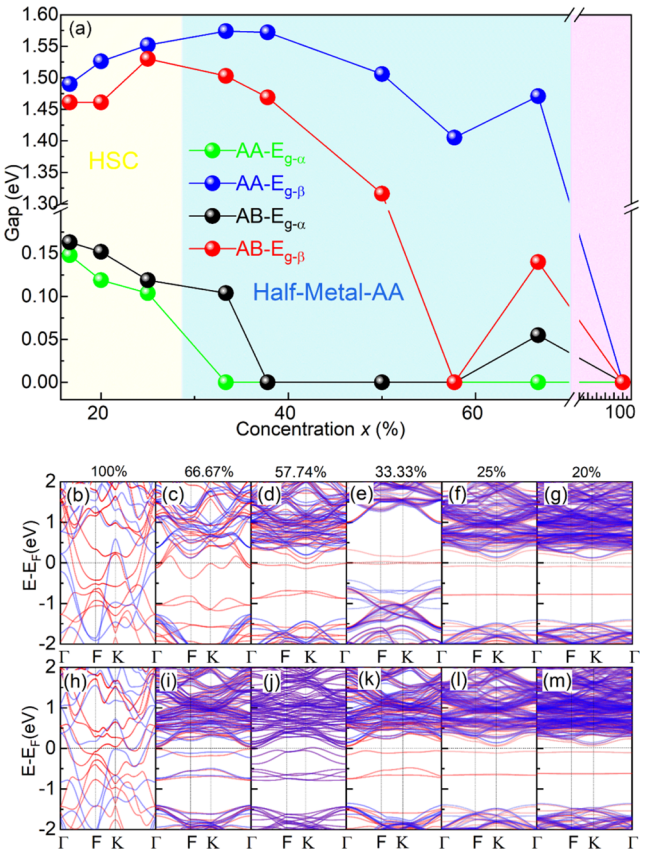

Figure 9. (a) E_g changes with x. The band structures of (b) Mo_3S_4, (c) $Mo_{20}S_{36}$, (d) Mo_7S_{12}, (e) $Mo_{19}S_{16}$, (f) $Mo_{19}S_{36}$, and (g) $Mo_{51}S_{100}$, with AA stackings, (h) Mo_3S_4, (i) $Mo_{20}S_{36}$, (j) Mo_7S_{12}, (k) $Mo_{19}S_{16}$, (l) $Mo_{19}S_{36}$, and (m) $Mo_{51}S_{100}$, with AB patterns.

the corresponding geometries are shown in Figure S3a−d. The band structures of 100% with AA and AB stackings are shown in Figure 9b,h, respectively. They are all normal spin-polarized metals. As the x values are reduced to 66.67 and 57.74% with AA patterns, the corresponding band structures are shown in Figure 9c,d, respectively. The spin-α's electrons behave as metals, while spin-β's electrons exhibit semiconducting properties with gaps of 1.471 (AA) and 1.405 (AB) eV, respectively. Therefore, $Mo_{20}S_{36}$ and Mo_7S_{12} with AA stacking are HMs, as shown in Figure 9a,c,d. However, $Mo_{20}S_{36}$-AB is a HSC with a direct band gap of 0.055 eV, as shown in Figure 9i. Moreover, the number of sub-bands of Mo_7S_{12}-AA stacking that cross the Fermi level and states at the Fermi level are also decreased as x is reduced. The states at the Fermi level are −3.682, −3.024, and 2.544 arb. unit^{-1} for 66.67, 57.74, and 50%, respectively. The spin-α electron of $Mo_{19}S_{36}$-AA stacking is metal, while the spin-β electron is a semiconductor with a direct band gap of 1.574 eV. It can be concluded that $Mo_{19}S_{36}$ is still HM. However, the $Mo_{19}S_{36}$-AB is HSC. The corresponding spin-α electron is a semiconductor with an indirect band gap of 0.112 eV, while the spin-β electron is also semiconducting with a direct band gap of 1.503 eV, as shown in Figure 9k. As x is further decreased to 25%, the corresponding $E_{g-\alpha}$ and $E_{g-\beta}$ is 0.119 (AA), 1.556 (AA), 0.124 (AB), and 1.530 (AB) eV,

https://doi.org/10.1021/acsaelm.4c00051
ACS Appl. Electron. Mater. 2024, 6, 4066−4079

respectively. The $E_{g-\alpha}$ and $E_{g-\beta}$ with 20% are 0.152 (AA), 1.526 (AA), 0.148 (AB), and 1.461 (AB) eV, respectively, as shown in Figure 9a,g,m, respectively. The introduction of Mo_{SI} atoms into Mo_mS_n creates new states within the gap, reducing the "original" band gap. When x is further decreased, the effect of Mo_{SI} atoms becomes "weaker" and the corresponding Mo_mS_n also transforms from HM into HSC.

In addition, the Mo_{SI} atoms could influence the planar averaged potential and work function of Mo_mS_n. The planar averaged potential and work function display a symmetrical pattern independent of the stacking orders. Compared with MoS_2 ML, the work function of Mo_mS_n is significantly reduced as Mo_{SI} atoms are inserted. More details can be found in Figures S15 and S16, respectively.

CONCLUSIONS

By analysis of SI-MoS_2, it can be concluded that Mo_{SI} can introduce a long-range magnetic order to nonmagnetic 2H-MoS_2. There is approximately one electron transfer from Mo_{SI} atoms to the connected S atoms, with the magnetic moment (MM) primarily localizing at the Mo_{SI} atoms. Mo_mS_n is HM with FM order after the SI of Mo atoms, at higher x. As x is further reduced, Mo_mS_n-AA(AB) is transferred into HSC. This shows that the superexchange interaction between Mo and S atoms is stronger than the direct exchange interaction between Mo_{SI} atoms. Furthermore, the EA of Mo_mS_n tends to IMA, independent of the stacking orders. The MAE of Mo_mS_n-AA and AB patterns differs, as the hybridization interaction between Mo's d orbitals is different. The formation energies also change with x and μ, and Mo_mS_n bonding with the Mo_{SI} atom is expected to be achieved under higher μ_{Mo}. Mo_mS_n show good dynamic and thermal stability at 300 and 600 K. These findings offer a promising approach to controlling the magnetic and electronic properties of 2H-MoS_2, which paves the use of MoS_2 and other TMDs in spintronics.

ASSOCIATED CONTENT

Supporting Information

The Supporting Information is available free of charge at https://pubs.acs.org/doi/10.1021/acsaelm.4c00051.

K-mesh test for MAE, geometries of MoS_2 BL, spin charge densities with different magnetic orders, band and PDOS of Mo_9S_{16}-AA and AB calculated by HSE06, the Mo d-orbital projected band structure and PDOS, band structure with SOC, spin charge densities of Mo_9S_{16} calculated by HSE06, spin charge densities of Mo_9S_{16}-AB, magnetic exchange parameters, AIMD of Mo_9S_{16} and $Mo_{33}S_{64}$ with NVT, geometries of Mo_3S_4-AA (AB), geometries with different x, spin densities and electronic properties of Mo_7S_{12} and $Mo_{19}S_{36}$, lattice parameters change with x, ε_f change with x and μ_S, k and c change with x, charge transfer change with x, planar averaged potential of Mo_mS_n, work function changes with x, detail of Monte Carlo simulation (PDF)

AUTHOR INFORMATION

Corresponding Author

Zhaoyong Guan − *Key Laboratory of Colloid and Interface Chemistry, Ministry of Education, School of Chemistry and Chemical Engineering, Shandong University, Jinan 250100 Shandong, P. R. China; School of Chemical Engineering, Shandong Institute of Petroleum and Chemical Technology, Dongying 257061 Shandong, P. R. China; School of Chemistry and Chemical Engineering, Shandong University, Jinan 250100, P. R. China;* orcid.org/0000-0002-6847-5809; Phone: +86-0531-88363179; Email: zyguan@sdu.edu.cn

Authors

Fangyu Zhang − *Key Laboratory of Colloid and Interface Chemistry, Ministry of Education, School of Chemistry and Chemical Engineering, Shandong University, Jinan 250100 Shandong, P. R. China; School of Chemistry and Chemical Engineering, Shandong University, Jinan 250100, P. R. China*

Linhui Lv − *Key Laboratory of Colloid and Interface Chemistry, Ministry of Education, School of Chemistry and Chemical Engineering, Shandong University, Jinan 250100 Shandong, P. R. China; School of Chemistry and Chemical Engineering, Shandong University, Jinan 250100, P. R. China*

Chao Jia − *Department of Chemical Physics & Hefei National Laboratory for Physical Sciences at Microscale, University of Science and Technology of China, Hefei 230026 Anhui, P. R. China*

Weiyi Wang − *Department of Chemical Physics & Hefei National Laboratory for Physical Sciences at Microscale, University of Science and Technology of China, Hefei 230026 Anhui, P. R. China*

Yanyan Jiang − *Key Laboratory for Liquid−Solid Structural Evolution & Processing of Materials (Ministry of Education), School of Materials Science and Engineering, Shandong University, Jinan 250061 Shandong, P. R. China;* orcid.org/0000-0002-7866-4689

Xingxing Li − *Department of Chemical Physics & Hefei National Laboratory for Physical Sciences at Microscale, University of Science and Technology of China, Hefei 230026 Anhui, P. R. China;* orcid.org/0000-0001-7820-0772

Ya Su − *School of Electrical Engineering, Shandong University, Jinan 250100 Shandong, P. R. China*

Complete contact information is available at: https://pubs.acs.org/10.1021/acsaelm.4c00051

Notes

The authors declare no competing financial interest.

ACKNOWLEDGMENTS

The authors thank Prof. Wenhui Duan for discussion of the evaluation of T_c, Prof. Bin Wang and Haidi Wang for discussion of the magnetic properties, Dr. Weinan Zhu and Prof. Akinwande, Deji for experimental realization of strains, Prof. Wen Zhao for discussion of the evaluation of formation energy, Prof. Wei Wei for discussion of the analysis of magnetic exchanged parameters, and Dr. Yang Li for discussion of the MCA calculation and LDA + U method. This work was supported by the financial support from the Natural Science Foundation of China (Grant No. 11904203), Natural Science Foundation of Shandong Province (Grant No. ZR2023MA019), and the Fundamental Research Funds of Shandong University (Grant No. 2019GN065). Dr. W.W. acknowledges the Postdoctoral Fellowship Program of China Postdoctoral Science Foundation (No. GZC20232540). The scientific calculations in this paper have been done on the HPC Cloud Platform of Shandong University and supercomputing center of USTC. The authors also acknowledge Beijing Super Cloud Computing Center (BSCC), Shanghai Supercomputer Center, and Tencent Quantum Laboratory for providing HPC

resources. Hefei Advanced Computing Center is acknowledged for computational support.

REFERENCES

(1) Butler, S. Z.; Hollen, S. M.; Cao, L.; Cui, Y.; Gupta, J. A.; Gutierrez, H. R.; Heinz, T. F.; Hong, S. S.; Huang, J.; Ismach, A. F.; Johnston-Halperin, E.; Kuno, M.; Plashnitsa, V. V.; Robinson, R. D.; Ruoff, R. S.; Salahuddin, S.; Shan, J.; Shi, L.; Spencer, M. G.; Terrones, M.; Windl, W.; Goldberger, J. E. Progress, Challenges, and Opportunities in Two-Dimensional Materials Beyond Graphene. *ACS Nano* **2013**, *7* (4), 2898−2926.

(2) Novoselov, K. S.; Geim, A. K.; Morozov, S. V.; Jiang, D.; Zhang, Y.; Dubonos, S. V.; Grigorieva, I. V.; Firsov, A. A. Electric Field Effect in Atomically Thin Carbon Films. *Science* **2004**, *306* (5696), 666−669.

(3) Xu, M.; Liang, T.; Shi, M.; Chen, H. Graphene-Like Two-Dimensional Materials. *Chem. Rev.* **2013**, *113* (5), 3766−3798.

(4) Butler, S. Z.; Hollen, S. M.; Cao, L.; Cui, Y.; Gupta, J. A.; Gutierrez, H. R.; Heinz, T. F.; Hong, S. S.; Huang, J.; Ismach, A. F.; Johnston-Halperin, E.; Kuno, M.; Plashnitsa, V. V.; Robinson, R. D.; Ruoff, R. S.; Salahuddin, S.; Shan, J.; Shi, L.; Spencer, M. G.; Terrones, M.; Windl, W.; Goldberger, J. E. Progress, Challenges, and Opportunities in Two-Dimensional Materials Beyond Graphene. *ACS Nano* **2013**, *7* (4), 2898−2926.

(5) Chopra, N. G.; Luyken, R. J.; Cherrey, K.; Crespi, V. H.; Cohen, M. L.; Louie, S. G.; Zettl, A. Boron Nitride Nanotubes. *Science* **1995**, *269* (5226), 966−967.

(6) Wang, Q. H.; Kalantar-Zadeh, K.; Kis, A.; Coleman, J. N.; Strano, M. S. Electronics and Optoelectronics of Two-Dimensional Transition Metal Dichalcogenides. *Nat. Nanotechnol.* **2012**, *7* (11), 699−712.

(7) Chhowalla, M.; Shin, H. S.; Eda, G.; Li, L.-J.; Loh, K. P.; Zhang, H. The Chemistry of Two-Dimensional Layered Transition Metal Dichalcogenide Nanosheets. *Nat. Chem.* **2013**, *5* (4), 263−275.

(8) Manzeli, S.; Ovchinnikov, D.; Pasquier, D.; Yazyev, O. V.; Kis, A. 2D Transition Metal Dichalcogenides. *Nat. Rev. Mater.* **2017**, *2* (8), No. 17033, DOI: 10.1038/natrevmats.2017.33.

(9) Mak, K. F.; Shan, J. Photonics and Optoelectronics of 2D Semiconductor Transition Metal Dichalcogenides. *Nat. Photonics* **2016**, *10* (4), 216−226.

(10) Wang, H. T.; Yuan, H. T.; Hong, S. S.; Li, Y. B.; Cui, Y. Physical and Chemical Tuning of Two-Dimensional Transition Metal Dichalcogenides. *Chem. Soc. Rev.* **2015**, *44* (9), 2664−2680.

(11) Khan, K.; Tareen, A. K.; Aslam, M.; Sagar, R. U. R.; Zhang, B.; Huang, W.; Mahmood, A.; Mahmood, N.; Khan, K.; Zhang, H.; Guo, Z. Recent Progress, Challenges, and Prospects in Two-Dimensional Photo-Catalyst Materials and Environmental Remediation. *Nano-Micro Lett.* **2020**, *12* (1), No. 167, DOI: 10.1007/s40820-020-00504-3.

(12) Han, W. Perspectives for Spintronics in 2D Materials. *APL Mater.* **2016**, *4* (3), No. 032401.

(13) Li, X.; Wu, X. Two-Dimensional Monolayer Designs for Spintronics Applications. *WIREs Comput. Mol. Sci.* **2016**, *6* (4), 441−455.

(14) Wu, Y.; Li, D.; Wu, C.-L.; Hwang, H. Y.; Cui, Y. Electrostatic Gating and Intercalation in 2D Materials. *Nat. Rev. Mater.* **2023**, *8* (1), 41−53.

(15) Novoselov, K. S.; Mishchenko, A.; Carvalho, A.; Neto, A. H. C. 2D Materials and Van Der Waals Heterostructures. *Science* **2016**, *353* (6298), No. aac9439, DOI: 10.1126/science.aac9439.

(16) Guan, Z. Y.; Ni, S.; Hu, S. L. Tunable Electronic and Optical Properties of Monolayer and Multilayer Janus MoSSe as a Photocatalyst for Solar Water Splitting: A First-Principles Study. *J. Phys. Chem. C* **2018**, *122* (11), 6209−6216.

(17) Guan, Z.; Ni, S. Strain-Controllable High Curie Temperature, Large Valley Polarization, and Magnetic Crystal Anisotropy in a 2D Ferromagnetic Janus VSeTe Monolayer. *ACS Appl. Mater. Interfaces* **2020**, *12* (47), 53067−53075.

(18) Radisavljevic, B.; Kis, A. Mobility Engineering and a Metal-Insulator Transition in Monolayer MoS_2. *Nat. Mater.* **2013**, *12* (9), 815−820.

(19) Zhao, Y. D.; Xu, K.; Pan, F.; Zhou, C. J.; Zhou, F. C.; Chai, Y. Doping, Contact and Interface Engineering of Two-Dimensional Layered Transition Metal Dichalcogenides Transistors. *Adv. Funct. Mater.* **2017**, *27* (19), No. 1603484, DOI: 10.1002/adfm.201603484.

(20) Mouri, S.; Miyauchi, Y.; Matsuda, K. Tunable Photoluminescence of Monolayer MoS_2 Via Chemical Doping. *Nano Lett.* **2013**, *13* (12), 5944−5948.

(21) Cheng, Y. C.; Zhu, Z. Y.; Mi, W. B.; Guo, Z. B.; Schwingenschlogl, U. Prediction of Two-Dimensional Diluted Magnetic Semiconductors: Doped Monolayer MoS_2 Systems. *Phy. Rev. B* **2013**, *87* (10), No. 100401, DOI: 10.1103/PhysRevB.87.100401.

(22) Mermin, N. D.; Wagner, H. Absence of Ferromagnetism or Antiferromagnetism in One- or Two-Dimensional Isotropic Heisenberg Models. *Phys. Rev. Lett.* **1966**, *17* (22), No. 1133, DOI: 10.1103/PhysRevLett.17.1133.

(23) Wan, J.; Lacey, S. D.; Dai, J.; Bao, W.; Fuhrer, M. S.; Hu, L. Tuning Two-Dimensional Nanomaterials by Intercalation: Materials, Properties and Applications. *Chem. Soc. Rev.* **2016**, *45* (24), 6742−6765.

(24) Ye, J. T.; Zhang, Y. J.; Akashi, R.; Bahramy, M. S.; Arita, R.; Iwasa, Y. Superconducting Dome in a Gate-Tuned Band Insulator. *Science* **2012**, *338* (6111), 1193−1196.

(25) Bao, W.; Fang, Z.; Wan, J.; Dai, J.; Zhu, H.; Han, X.; Yang, X.; Preston, C.; Hu, L. Aqueous Gating of Van Der Waals Materials on Bilayer Nanopaper. *ACS Nano* **2014**, *8* (10), 10606−10612.

(26) Yao, J.; Koski, K. J.; Luo, W.; Cha, J. J.; Hu, L.; Kong, D.; Narasimhan, V. K.; Huo, K.; Cui, Y. Optical Transmission Enhacement through Chemically Tuned Two-Dimensional Bismuth Chalcogenide Nanoplates. *Nat. Commun.* **2014**, *5* (1), No. 5670.

(27) Chen, K. P.; Chung, F. R.; Wang, M.; Koski, K. J. Dual Element Intercalation into 2D Layered Bi_2Se_3 Nanoribbons. *J. Am. Chem. Soc.* **2015**, *137* (16), 5431−5437.

(28) Bointon, T. H.; Khrapach, I.; Yakimova, R.; Shytov, A. V.; Craciun, M. F.; Russo, S. Approaching Magnetic Ordering in Graphene Materials by $FeCl_3$ Intercalation. *Nano Lett.* **2014**, *14* (4), 1751−1755.

(29) Guan, Z.; Lv, L.; An, Z.; Jiang, Y.; Su, Y. Tailing the Magnetoelectric Properties of $Cr_2Ge_2Te_6$ by Engineering Covalently Bonded Cr Self-Intercalation: Ferromagnetic Half-Metal. *ACS Appl. Electron. Mater.* **2023**, *5* (6), 2999−3009.

(30) Balandin, A. A. Thermal Properties of Graphene and Nanostructured Carbon Materials. *Nat. Mater.* **2011**, *10* (8), 569−581.

(31) Acerce, M.; Voiry, D.; Chhowalla, M. Metallic 1t Phase MoS2 Nanosheets as Supercapacitor Electrode Materials. *Nat. Nanotechnol.* **2015**, *10* (4), 313−318.

(32) Zhao, X.; Song, P.; Wang, C.; Riis-Jensen, A. C.; Fu, W.; Deng, Y.; Wan, D.; Kang, L.; Ning, S.; Dan, J.; Venkatesan, T.; Liu, Z.; Zhou, W.; Thygesen, K. S.; Luo, X.; Pennycook, S. J.; Loh, K. P. Engineering Covalently Bonded 2D Layered Materials by Self-Intercalation. *Nature* **2020**, *581* (7807), 171−177.

(33) Yin, Y.; Lian, C.-S.; Meng, F.; Liu, Y.; Chen, W.; Ji, L.; Zhou, X.; Zhang, Z.; Zhang, Q.; Gu, L.; Duan, W.; Xue, Q.-K.; Chen, X.; Ji, S.-H. Quenched Charge Density Wave and Large in-Plane Upper Critical Field of Self-Intercalated Bilayer $NbSe_2$. *Phys. Rev. B* **2023**, *108* (4), No. L041405.

(34) Niu, K.; Qiu, G.; Wang, C.; Li, D.; Niu, Y.; Li, S.; Kang, L.; Cai, Y.; Han, M.; Lin, J. Self-Intercalated Magnetic Heterostructures in 2D Chromium Telluride. *Adv. Funct. Mater.* **2023**, *33* (2), No. 2208528.

(35) Guan, Z.; Lv, L.; An, Z.; Su, Y.; Jiang, Y.; Wu, X.; Ni, S. Van Der Waals Stacked 2D-Layered $Co_2Ge_2Te_6$ with High Curie Temperature and Large Magnetic Crystal Anisotropy. *J. Phys. Chem. C* **2023**, *127* (12), 5991−6001.

(36) Xiong, Y. Engineering Two-Dimensional Magnets at Birth. *Nat. Electron.* **2022**, *5* (4), 197−198.

https://doi.org/10.1021/acsaelm.4c00051
ACS Appl. Electron. Mater. 2024, 6, 4066−4079

(37) Guo, Y.; Liu, N.; Zhao, Y.; Jiang, X.; Zhou, S.; Zhao, J. Enhanced Ferromagnetism of CrI_3 Bilayer by Self-Intercalation. *Chin. Phys. Lett.* **2020**, *37* (10), No. 107506.
(38) Li, R.; Jiang, J.; Bai, H.; Mi, W. Tailoring Interlayer Magnetic Coupling to Modify the Magnetic Properties of $FeCl_2$ Bilayers by Self-Intercalation. *J. Mater. Chem. C* **2022**, *10* (40), 14955−14962.
(39) Niu, J.; Yan, B.; Ji, Q.; Liu, Z.; Li, M.; Gao, P.; Zhang, Y.; Yu, D.; Wu, X. Anomalous Hall Effect and Magnetic Orderings in Nanothick V_5S_8. *Phys. Rev. B* **2017**, *96* (7), No. 075402.
(40) Huang, M.; Gao, L.; Zhang, Y.; Lei, X.; Hu, G.; Xiang, J.; Zeng, H.; Fu, X.; Zhang, Z.; Chai, G.; Peng, Y.; Lu, Y.; Du, H.; Chen, G.; Zang, J.; Xiang, B. Possible Topological Hall Effect above Room Temperature in Layered $Cr_{1.2}Te_2$ Ferromagnet. *Nano Lett.* **2021**, *21* (10), 4280−4286.
(41) Jin, Z.; Ji, Z.; Zhong, Y.; Jin, Y.; Hu, X.; Zhang, X.; Zhu, L.; Huang, X.; Li, T.; Cai, X.; Zhou, L. Controlled Synthesis of a Two-Dimensional Non-Van Der Waals Ferromagnet toward a Magnetic Moiré Superlattice. *ACS Nano* **2022**, *16* (5), 7572−7579.
(42) Huang, M.; Ma, Z. W.; Wang, S.; Li, S.; Li, M.; Xiang, J. X.; Liu, P.; Hu, G. J.; Zhang, Z. M.; Sun, Z.; Lu, Y. L.; Sheng, Z. G.; Chen, G.; Chueh, Y. L.; Yang, S. Y.; Xiang, B. Significant Perpendicular Magnetic Anisotropy in Room-Temperature Layered Ferromagnet of Cr-Intercalated $CrTe_2$. *2D Mater.* **2021**, *8* (3), No. 031003, DOI: 10.1088/2053-1583/abfaae.
(43) Tang, B.; Wang, X.; Han, M.; Xu, X.; Zhang, Z.; Zhu, C.; Cao, X.; Yang, Y.; Fu, Q.; Yang, J.; Li, X.; Gao, W.; Zhou, J.; Lin, J.; Liu, Z. Phase Engineering of Cr_5Te_8 with Colossal Anomalous Hall Effect. *Nat. Electron.* **2022**, *5* (4), 224−232.
(44) Saha, R.; Meyerheim, H. L.; Göbel, B.; Hazra, B. K.; Deniz, H.; Mohseni, K.; Antonov, V.; Ernst, A.; Knyazev, D.; Bedoya-Pinto, A.; Mertig, I.; Parkin, S. S. P. Observation of Néel-Type Skyrmions in Acentric Self-Intercalated $Cr_{1+\delta}Te_2$. *Nat. Commun.* **2022**, *13* (1), No. 3965.
(45) Lasek, K.; Coelho, P. M.; Gargiani, P.; Valvidares, M.; Mohseni, K.; Meyerheim, H. L.; Kostanovskiy, I.; Zberecki, K.; Batzill, M. Van Der Waals Epitaxy Growth of 2D Ferromagnetic $Cr_{(1+\delta)}Te_2$ Nanolayers with Concentration-Tunable Magnetic Anisotropy. *Appl. Phys. Rev.* **2022**, *9* (1), No. 011409, DOI: 10.1063/5.0070079.
(46) Pan, S.; Hong, M.; Zhu, L.; Quan, W.; Zhang, Z.; Huan, Y.; Yang, P.; Cui, F.; Zhou, F.; Hu, J.; Zheng, F.; Zhang, Y. On-Site Synthesis and Characterizations of Atomically-Thin Nickel Tellurides with Versatile Stoichiometric Phases through Self-Intercalation. *ACS Nano* **2022**, *16* (7), 11444−11454.
(47) Liu, Z.; Wang, L.; Hong, Y.-L.; Chen, X.-Q.; Cheng, H.-M.; Ren, W. Two-Dimensional Superconducting $MoSi_2N_4(MoN)_{4n}$ Homologous Compounds. *Nat. Sci. Rev.* **2022**, *10* (4), No. nwac273, DOI: 10.1093/nsr/nwac273.
(48) Zhang, Z.-M.; Gong, B.-C.; Nie, J.-H.; Meng, F.; Zhang, Q.; Gu, L.; Liu, K.; Lu, Z.-Y.; Fu, Y.-S.; Zhang, W. Self-Intercalated 1T-$FeSe_2$ as an Effective Kagome Lattice. *Nano Lett.* **2023**, *23* (3), 954−961.
(49) Huan, Y.; Luo, T.; Han, X.; Ge, J.; Cui, F.; Zhu, L.; Hu, J.; Zheng, F.; Zhao, X.; Wang, L.; Wang, J.; Zhang, Y. Composition-Controllable Syntheses and Property Modulations from 2D Ferromagnetic Fe_5Se_8 to Metallic Fe_3Se_4 Nanosheets. *Adv. Mater.* **2023**, *35* (1), No. 2207276.
(50) Wu, F.; Yao, X.; Liu, Y.; Zhu, X.; Lu, J.; Zhou, W.; Zhang, X. TMB_{12}: A Newly Designed 2D Transition-Metal Boride for Spintronics and Electrochemical Catalyst Applications. *Nanoscale* **2023**, *15* (5), 2079−2086.
(51) Luo, T.; Zhang, M.; Shi, J.; Zheng, F. Emergent Charge Density Wave Featuring Quasi-One-Dimensional Chains in Ta-Intercalated Bilayer 2H-TaS_2 with Coexisting Superconductivity. *Phys. Rev. B* **2023**, *107* (16), No. L161401.
(52) Wang, F.; Zhang, Y.; Wang, Z.; Zhang, H.; Wu, X.; Bao, C.; Li, J.; Yu, P.; Zhou, S. Ionic Liquid Gating Induced Self-Intercalation of Transition Metal Chalcogenides. *Nat. Commun.* **2023**, *14* (1), No. 4945.
(53) Bai, H.; Wu, Q.; Ai, H.; Liu, D.; Feng, J.; Ang, L. K.; Lu, Y.; Yang, M.; Pan, H. Interlayer-Incorporation of MoS_2 (TM-MoS_2) to Achieve Unique Magnetic and Electronic Properties for Spintronics. *Adv. Electron. Mater.* **2022**, *8* (10), No. 2200209.
(54) Zhang, Y.; Ding, W.; Chen, Z.; Guo, J.; Pan, H.; Li, X.; Zhao, Z.; Liu, Y.; Xie, W. Layer-Dependent Magnetism in Two-Dimensional Transition-Metal Chalcogenides M_nT_{n+1} (M = V, Cr, and Mn; T = S, Se, and Te; and N = 2, 3, and 4). *J. Phys. Chem. C* **2021**, *125* (15), 8398−8406.
(55) Li, Q.-Q.; Li, S.; Wu, D.; Ding, Z.-K.; Cao, X.-H.; Huang, L.; Pan, H.; Li, B.; Chen, K.-Q.; Duan, X.-D. Magnetic Properties Manipulation of $CrTe_2$ Bilayer through Strain and Self-Intercalation. *Appl. Phys. Lett.* **2021**, *119* (16), No. 162402, DOI: 10.1063/5.0068018.
(56) Huang, X.; Mo, Y.; Xu, J.; Hu, J.; Nie, X.; Chen, C.; Liu, J.; Jiang, X.; Liu, J.-M. Fe-Intercalated Fe_3GeTe_2: Potential Quasi-Van Der Waals Magnets. *Appl. Phys. Lett.* **2023**, *123* (1), No. 012405, DOI: 10.1063/5.0152869.
(57) Huang, H.-C.; Wang, T.-T.; Li, J.; Chen, J.; Bu, Y.; Cheng, S.-B. A Strain-Engineered Self-Intercalation Ta_9Se_{12} Based Bifunctional Single Atom Catalyst for Oxygen Evolution and Reduction Reactions. *Appl. Surf. Sci.* **2022**, *602*, No. 154378.
(58) Hu, Y.; Rogée, L.; Wang, W.; Zhuang, L.; Shi, F.; Dong, H.; Cai, S.; Tay, B. K.; Lau, S. P. Extendable Piezo/Ferroelectricity in Nonstoichiometric 2D Transition Metal Dichalcogenides. *Nat. Commun.* **2023**, *14* (1), No. 8470.
(59) Kresse, G.; Furthmuller, J. Efficiency of Ab-Initio Total Energy Calculations for Metals and Semiconductors Using a Plane-Wave Basis Set. *Comput. Mater. Sci.* **1996**, *6* (1), 15−50.
(60) Perdew, J. P.; Burke, K.; Ernzerhof, M. Generalized Gradient Approximation Made Simple. *Phys. Rev. Lett.* **1996**, *77* (18), No. 3865, DOI: 10.1103/PhysRevLett.77.3865.
(61) Heyd, J.; Scuseria, G. E.; Ernzerhof, M. Hybrid Functionals Based on a Screened Coulomb Potential. *J. Chem. Phys.* **2003**, *118* (18), 8207−8215.
(62) Heyd, J.; Scuseria, G. E.; Ernzerhof, M. Erratum: "Hybrid Functionals Based on a Screened Coulomb Potential" [J. Chem. Phys. 118, 8207 (2003)]. *J. Chem. Phys.* **2006**, *124* (21), No. 219906.
(63) Liechtenstein, A. I.; Anisimov, V. V.; Zaanen, J. Density-Functional Theory and Strong Interactions: Orbital Ordering in Mott-Hubbard Insulators. *Phys. Rev. B* **1995**, *52* (8), No. R5467, DOI: 10.1103/PhysRevB.52.R5467.
(64) Ataca, C.; Şahin, H.; Ciraci, S. Stable, Single-Layer MX_2 Transition-Metal Oxides and Dichalcogenides in a Honeycomb-Like Structure. *J. Phys. Chem. C* **2012**, *116* (16), 8983−8999.
(65) Monkhorst, H. J.; Pack, J. D. Special Points for Brillouin-Zone Integrations. *Phys. Rev. B* **1976**, *13* (12), 5188−5192.
(66) Togo, A.; Tanaka, I. First Principles Phonon Calculations in Materials Science. *Scr. Mater.* **2015**, *108*, 1−5.
(67) Nosé, S. A Unified Formulation of the Constant Temperature Molecular Dynamics Methods. *J. Chem. Phys.* **1984**, *81* (1), 511−519.
(68) Lou, F.; Li, X. Y.; Ji, J. Y.; Yu, H. Y.; Feng, J. S.; Gong, X. G.; Xiang, H. J. PASP: Property Analysis and Simulation Package for Materials. *J. Chem. Phys.* **2021**, *154*, No. 114103.
(69) Grimme, S. Semiempirical GGA-Type Density Functional Constructed with a Long-Range Dispersion Correction. *J. Comput. Chem.* **2006**, *27* (15), 1787−1799.
(70) Henkelman, G.; Arnaldsson, A.; Jónsson, H. A Fast and Robust Algorithm for Bader Decomposition of Charge Density. *Comput. Mater. Sci.* **2006**, *36* (3), 354−360.
(71) An, Z. Y.; Su, Y.; Ni, S.; Guan, Z. Y. Carrier Doping Modulates 2D Intrinsic Ferromagnetic $Mn_2Ge_2Te_6$ Monolayer, High Curie Temperature, Large Magnetic Crystal Anisotropy. *J. Phys. Chem. C* **2022**, *126* (27), 11330−11340.
(72) Li, D.; Smogunov, A.; Barreteau, C.; Ducastelle, F.; Spanjaard, D. Magnetocrystalline Anisotropy Energy of Fe(001) and Fe(110) Slabs and Nanoclusters: A Detailed Local Analysis within a Tight-Binding Model. *Phys. Rev. B* **2013**, *88* (21), No. 214413.
(73) Li, D.; Barreteau, C.; Castell, M. R.; Silly, F.; Smogunov, A. Out- Versus in-Plane Magnetic Anisotropy of Free Fe and Co

Nanocrystals: Tight-Binding and First-Principles Studies. *Phys. Rev. B* **2014**, *90* (20), No. 205409.
(74) Wang, D.-s.; Wu, R.; Freeman, A. J. First-Principles Theory of Surface Magnetocrystalline Anisotropy and the Diatomic-Pair Model. *Phys. Rev. B* **1993**, *47* (22), No. 14932, DOI: 10.1103/PhysRevB.47.14932.
(75) Yang, B. S.; Zhang, J.; Jiang, L. N.; Chen, W. Z.; Tang, P.; Zhang, X. G.; Yan, Y.; Han, X. F. Strain Induced Enhancement of Perpendicular Magnetic Anisotropy in Co/Graphene and Co/BN Heterostructures. *Phys. Rev. B* **2017**, *95* (17), No. 174424.
(76) Ke, L. Q.; van Schilfgaarde, M. Band-Filling Effect on Magnetic Anisotropy Using a Green's Function Method. *Phys. Rev. B* **2015**, *92* (1), No. 014423.

https://doi.org/10.1021/acsaelm.4c00051
ACS Appl. Electron. Mater. 2024, 6, 4066−4079